Exceptional points in time-varying oscillators with enhanced sensing sensitivity

Yabin Jin,[1,2,*] Wenjun Li,[3] Bahram Djafari-Rouhani,[4] Daniel Torrent,[5] Yanxun Xiang,[1,†] and Fu-Zhen Xuan[1]

[1]*Shanghai Key Laboratory of Intelligent Sensing and Detection Technology, School of Mechanical and Power Engineering, East China University of Science and Technology, 200237 Shanghai, China*
[2]*Shanghai Institute of Aircraft Mechanics and Control, 200092 Shanghai, China*
[3]*School of Aerospace Engineering and Applied Mechanics, Tongji University, 200092 Shanghai, China*
[4]*Institut d'Electronique, de Microélectonique et de Nanotechnologie, UMR CNRS 8520, Département de Physique, Université de Lille, 59650 Villeneuve d'Ascq, France*
[5]*Grup de Recerca óptica de Castelló (GROC), Institut de Noves Tecnologies de la Imatge (INIT), Universitat Jaume I, Castelló de la Plana, 12071, Spain*

We explore the exceptional points (EPs) in mass-spring oscillators with time-varying stiffness. The second-order EPs result from the coalescences of the fundamental and harmonic eigenmodes that can be achieved by a time modulation of the spring stiffness. The occurrence of EPs is first demonstrated in a theoretical model by solving the eigenvalue problem with the state-space method. The signature of the EP can be seen in the response spectrum when the system is subjected to an external excitation. The undamped and damped cases are both considered in this mass-spring oscillator, and the impact of the damping ratio and modulation amplitude on the EPs is systematically investigated. Based on an analogy of the equation of motion with the Mathieu differential equation, we discuss the stability of the undamped time-varying system under different modulation parameters and explore its connection to the EP phenomenon. As a typical property of a second-order EP, the square-root dependence of the frequency splitting response to a perturbation is studied by introducing an added mass. In a second part, the above theoretical concepts are established by simulation methods in an elastic solid mass-spring model and an equivalent time-varying stiffness is realized by shunting a piezoelectric patch with switch-controlled external negative capacitance circuits. This work should pave the way for applications of crack or perturbation detection in elastic media and inspire other elastic wave modulation functions in time-varying systems.

I. INTRODUCTION

In the field of wave physics, increasing attention is being paid to the study of non-Hermitian systems, which are closer to reality in terms of energy exchange than conservative Hermitian systems [1–3]. The introduction of gain and loss results in complex parameters of the systems, exhibiting unusual physical properties and wave effects [4–7]. The exceptional point (EP) is a non-Hermitian degeneracy where the spectrum is transformed from pure real to complex conjugate [8], which reflects the simultaneous coalescence of the eigenfrequencies and eigenmodes in a finite structure [9–11] and of the eigenvalues and eigenvectors of the scattering matrix in a waveguide structure [12,13]. Most studies on EPs are based on parity-time (*PT*) symmetric systems with balanced gain and loss and the EP

represents the transition point from symmetry being conserved to being broken [7,14,15]. There are many related studies of intriguing properties and applications, such as unidirectional invisibility [16,17], laser mode selectivity [18], asymmetric mode switching [19], and enhanced sensitivity [20–22].

Recently, the sensitive response of EPs to perturbations has attracted increasing attention for high-precision sensing applications [23]. It has been demonstrated that a tiny perturbation of an *n*th-order-EP system can cause lifted degeneracy, resulting in frequency splitting behaving as the *n*th root of the perturbation, and thus a response that is superior to the linear response in a Hermitian system [24–26]. This has inspired many detection and sensing methods based on EPs, for instance, nanoparticle detection in a microcavity [27–29], crack detection in elastic media [25,30], deposited mass detection [9,22], and the sensing of minor changes of a coupling capacitor in a sixth-order-EP circuit [31]. These methods are all

---

*Contact author: yabin.jin@ecust.edu.cn
†Contact author: yxxiang@ecust.edu.cn

established in time-invariant systems, without time being set as a modulation parameter. However, introducing time as an independent variable will give wave regulation a new degree of freedom. For instance, in artificial structures, research on temporal or spatiotemporal modulation structures is emerging with many functional applications [32–36], such as frequency conversion [37], nonreciprocal mode transition [38], nonreciprocal wave propagation [39–44], parametric amplification [45], and unidirectional amplification [46].

The EP phenomenon with time modulation in finite structures has been the subject of a few investigations. Recently, Kazemi *et al.* proposed an *LC* circuit with periodic time variation for EP construction and theoretically derived the EP's existence condition without gain and loss elements [47]. Only one resonator is needed to construct the EP in the time-modulated system, in contrast to the *PT*-symmetric system where two coupled resonators are needed to produce gain and loss effects. This design route inspired Yuan *et al.* to perform an analogous scheme in a mechanical system, namely a resonant structure with time-varying mass, that demonstrates the existence of an EP and the capability for detecting defects in elastic materials [48]. Koutserimpas *et al.* studied a temporally dependent dynamic medium interacting with electromagnetic waves and linked the resulting energy transitions with EP theory [49]. Multiphysical interaction is a common way to practically design time-modulated elastic structures and realize abnormal wave effects. A few examples are an elastic beam with an integrated shunted piezoelectric patch array [50,51], stiffness variations induced by motor-driven geometrically phase-shifted resonators [43], and an elastic beam embedded with ac-programming permanent magnets [52]. Trainiti *et al.* proposed a practical scheme to experimentally implement stiffness modulation via shunted piezoelectric patches controlled by a switching circuit and realized the frequency-selective reflection of a waveguide [53]. For a deeper understanding of the effect of time-modulated parameters on mechanical resonances, the conditions and mechanisms that induce EPs should be further explored.

In this work, based on the concept of modulating the stiffness of piezoelectric patches, we devised an equivalent piezoelectric spring with time-varying stiffness which we used to explore the EP phenomenon and its application for the detection of small perturbations. This design is based on the prior development of a theoretical mass-spring model that we explain first. The manuscript is organized as follows. In Sec. II, we theoretically derive the EP's existence for the mechanical oscillator with time-varying stiffness by the state-space method. In Sec. III, we combine the Mathieu equation to derive the stability condition of the undamped time-varying system, and discuss the relationship between the EP and the stability threshold during parameter modulation. In Sec. IV, the response spectra

under an external excitation are obtained with both a theoretical and a simulated model. In Sec. V, we introduce a constant damping into the time-varying system and investigate its influence on the EPs and spectral responses. In Sec. VI, we explore the detection capability of the design at the EP by adding a small perturbing mass, and demonstrate the square-root behavior of the frequency splitting by both theoretical calculation and simulation. Section VII proposes a practical scheme with a shunted piezoelectric patch to realize the EP and perturbation detection. Finally, we summarize this work in Sec. VIII.

II. EP INDUCED BY AN OSCILLATOR WITH TIME-VARYING STIFFNESS

We consider a mass-spring mechanical oscillator with mass M and time-varying stiffness $K(t)$, as shown in Fig. 1(a). The time variable is introduced in the cosine form as $K(t) = K_0[1 + \alpha \cos(\omega_m t)]$, where α and ω_m represent the modulation amplitude and the modulation frequency, K_0 is the original stiffness, and $\omega_0 = \sqrt{K_0/M}$ the natural frequency. To obtain the evolution of the eigenfrequencies of the time-modulated system, we use the state-space method to solve the eigenvalue problem [48]. The equation of motion of the system can be written as follows:

$$M \frac{d^2 u(t)}{dt^2} + K(t)u(t) = 0. \qquad (1)$$

We choose two independent state variables to describe the two-level system; namely, the state vector is $\mathbf{s} = [du/dt, u]^T$. Then Eq. (1) can be equivalently given by the following state function:

$$\frac{d}{dt}\mathbf{s}(t) = \mathbf{H}(t)\mathbf{s}(t), \qquad (2)$$

with

$$\mathbf{H}(t) = \begin{bmatrix} 0 & -\dfrac{1}{M}K(t) \\ 1 & 0 \end{bmatrix}. \qquad (3)$$

The state vector changing from t_0 to t can be expressed as $\mathbf{s}(t) = \mathbf{T}(t, t_0)\mathbf{s}(t_0)$, where $\mathbf{T}(t, t_0)$ is the state transition matrix, and note that $\mathbf{T}(t_0, t_0) = \mathbf{I}$ ($\mathbf{I}$ is the unit matrix of rank 2). By substituting the state vector into Eq. (2), the evolution of the equation of motion can be obtained as follows:

$$\frac{d}{dt}\mathbf{T}(t, t_0) = \mathbf{H}(t)\mathbf{T}(t, t_0). \qquad (4)$$

If we consider the evolution in one modulation period (t, $t + T$) with $T = 2\pi/\omega_m$, the state vector can be similarly
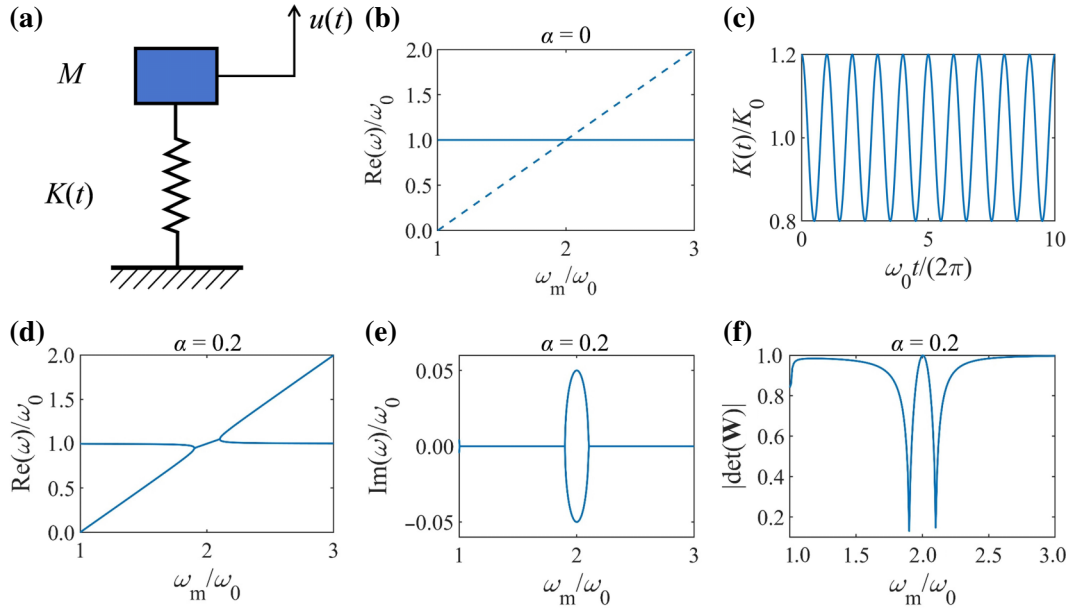
FIG. 1. (a) Schematic of the mass-spring model with constant mass M and time-varying stiffness $K(t)$. (b) The variation of the real parts of the eigenfrequencies as a function of ω_m/ω_0 with modulation amplitude $\alpha = 0$. (c) Schematic of the time-varying stiffness with $\alpha = 0.2$. The variation of the (d) real and (e) imaginary parts of the eigenfrequencies and (f) $|\det(\mathbf{W})|$ ($\mathbf{W}$ is the associated eigenvector matrix) as a function of ω_m/ω_0 when $\alpha = 0.2$.

given as follows:

$$\mathbf{s}(t + T) = \mathbf{T}(t + T, t)\mathbf{s}(t). \tag{5}$$

When we divide the period T into N portions at intervals of $\delta = T/N$, for each portion of (t_i, t_{i+1}) (with $i = 1, 2, \ldots, N$), we have $\mathbf{s}(t_{i+1}) = \mathbf{T}(t_{i+1}, t_i)\mathbf{s}(t_i)$. If δ is small enough, we can express $\mathbf{T}(t_{i+1}, t_i)$ in the form of the Taylor expansion as follows:

$$\mathbf{T}(t_{i+1}, t_i) = \mathbf{T}(t_{i+1}, t_i)|_{t_i} + \delta \left.\frac{d\mathbf{T}(t_{i+1}, t_i)}{dt}\right|_{t_i}$$
$$+ \frac{\delta^2}{2!} \left.\frac{d^2\mathbf{T}(t_{i+1}, t_i)}{dt^2}\right|_{t_i} + o(\delta^2). \tag{6}$$

By substituting Eq. (4) into Eq. (6) and ignoring the high-order terms of δ, we obtain

$$\mathbf{T}(t_{i+1}, t_i) = \mathbf{I} + \delta\mathbf{H}(t_i) + \frac{\delta^2}{2!}\left[\mathbf{H}^2(t_i) + \frac{d}{dt}\mathbf{H}(t_i)\right]. \tag{7}$$

Within a modulation period T, the state transition matrix is given by

$$\mathbf{T}(t + T, t) = \prod_{i=1}^{N} \mathbf{T}(t_{N-i+2}, t_{N-i+1}). \tag{8}$$

As a periodically time-varying system, the solution satisfies the Bloch theorem given by

$$\mathbf{s}(t + T) = e^{i\omega T}\mathbf{s}(t), \tag{9}$$

where ω is the mass vibration's complex eigenfrequency of a Floquet harmonic. From Eqs. (5) and (9), we have

$$\mathbf{T}(t + T)\mathbf{s}(t) = e^{i2\pi\omega/\omega_m}\mathbf{s}(t). \tag{10}$$

When $\Omega(\omega/\omega_m) = e^{i2\pi\omega/\omega_m}$, the eigenfrequency and eigenvector can be obtained by solving $\det(\mathbf{T}(\omega_m) - \Omega(\omega/\omega_m)\mathbf{I}) = 0$. The corresponding periodic solutions are given by $\Omega(\omega) = \Omega(\omega + k\omega_m)$, where k is an integer. In the following, we call $\mathbf{W}$ the matrix constructed from the eigenvectors of the structure.

In the following calculations, we set $N = 1000$ steps. First, we discuss the case of a constant stiffness with $\alpha = 0$. As shown in Fig. 1(b), we display the evolution of the real eigenfrequencies ω versus the modulation frequency ω_m represented in dimensionless units. The horizontal curve with $\omega/\omega_0 = 1$ corresponds to the fundamental frequency, while the inclined dashed curve would represent the first-order harmonic if the amplitude α were not strictly equal to zero. These two curves exhibit an intersection at $\omega_m/\omega_0 = 2$ and $\omega/\omega_0 = 1$.

When setting the stiffness as a time-dependent variable, we find that the eigenfrequencies coalesce at a certain modulation frequency range. As an example, in Fig. 1(c), we set the stiffness to vary harmonically with modulation amplitude $\alpha = 0.2$. By solving the eigenvalue problem in the

sweeping range of ω_m/ω_0 from 1 to 3 (a broader range is discussed in Appendix A), we obtain the real and imaginary parts of the eigenfrequencies as shown in Figs. 1(d) and 1(e), respectively. It is found that as ω_m increases, the bifurcated real eigenfrequency branches coalesce at $\omega_m/\omega_0 = 1.9$ and $\omega/\omega_0 = 0.95$, while, the imaginary parts of the eigenfrequencies become nonzero from this coalescence point. In addition, the determinant of the matrix **W** reaches a minimum and approaches zero at the coalescence point [Fig. 1(f)], which demonstrates the EP behavior. The transition of the real eigenfrequencies from coalescence to rebifurcation appears at the second EP at $\omega_m/\omega_0 = 2.1$ and $\omega/\omega_0 = 1.05$ where the imaginary parts of the eigenfrequencies turn to zero and the determinant of the eigenvector reaches a new dip. Note that the branch of the eigenfrequency close to ω_0 corresponds to the fundamental mode, while the other inclined branch corresponds to the first-order harmonic mode [48]. The periodic solutions with a wider sweeping range of ω_m/ω_0 from 0 to 3 and eigenfrequency range of ω/ω_0 from 0 to 11 are presented in Appendix A, where we can see multiple EPs when ω_m/ω_0 is less than 1. The real parts of the complex eigenfrequencies have a period of ω_m between two harmonic orders according to $\Omega(\omega) = \Omega(\omega + k\omega_m)$, and the imaginary parts are identical, which indicates the same rate of growth or decay for each resonance.

III. STABILITY ANALYSIS OF THE TIME-VARYING SYSTEM USING THE MATHIEU EQUATION

The Mathieu equation describes a kind of system with periodic parameters and can be used in the stability analysis of nonlinear vibrations. In relation to our time-varying system, the cosine time-modulated stiffness acts as the periodic part of the Mathieu equation, which may cause instability under some parameter combinations [45,54, 55]. We discuss the stability under different modulation parameters and further explore its connection with the EP phenomenon. First, we perform the following variable substitutions to the equation of motion [Eq. (1)]: $\tau = \omega_m t$, $\lambda = \omega_0^2/\omega_m^2$, $\xi = \alpha\omega_0^2/\omega_m^2$. Then Eq. (1) can be expressed as follows:

$$\frac{d^2 u}{d\tau^2} + [\lambda + \xi \cos(\tau)]u = 0. \tag{11}$$

Equation (11) is the classical form of the Mathieu equation where $[\lambda + \xi \cos(\tau)]$ is the periodic part. The transition curve in the λ-ξ plane is introduced to represent stability changes of the solutions [55], as defined in Eq. (12). During one period of $0 \le \tau \le 2\pi$, we can obtain the solutions at the end of the period under two types of initial conditions: when $[u,\ du/d\tau]_{\tau=0} = [1, 0]$, one gets $u_1(\tau = 2\pi)$; when $[u,\ du/d\tau]_{\tau=0} = [0, 1]$, one gets $u_2(\tau = 2\pi)$. Then, we

can build the following modulus expression with matrix

$$C = \begin{bmatrix} u_1(\tau) & u_2(\tau) \\ du_1(\tau)/d\tau & du_2(\tau)/d\tau \end{bmatrix}$$

as

$$g = |\text{tr}C\,|_{\tau=2\pi}|. \tag{12}$$

As a function of the parameter in the physical problem, Eq. (12) defines a condition to distinguish the stability (when $g < 2$) and instability (when $g > 2$) of the system, separated by the transition curve (when $g = 2$), where g is the criterion that reflects the system's stability states. The stability is determined by the eigenvalues of

$$C = \begin{bmatrix} u_1(\tau) & u_2(\tau) \\ du_1(\tau)/d\tau & du_2(\tau)/d\tau \end{bmatrix},$$

which can be solved as $\left(\text{tr}C \pm \sqrt{\text{tr}C^2 - 4}\right)/2$ (see Ref. [55] for a detailed discussion). If g is larger than 2, we can obtain two positive roots with one root's modulus less than unity and the other larger than unity, resulting in an unstable case. If g is less than 2, both roots are complex and unitary, resulting in a stable case.

The stability evaluation of the Mathieu differential equation, Eq. (11), is based on an eigenvalue analysis that does not need an external excitation. In Fig. 2(a), the unstable domain is highlighted in cyan, while the system is stable in the white area, showing the criterion for system stability. However, to illustrate the dynamical behavior of the system over time, it is necessary to apply a source and perform a time-domain analysis. The source-response results depict the displacement variation with time and further demonstrate whether the system is stable or not. We apply an excitation force to the mass with the form of $F(t) = A \sin(\omega_c t)$, where A is the excitation amplitude, set as 1, and ω_c is the excitation frequency, set as $1.5\omega_0$. The choice of the latter frequency is motivated by the fact that it allows an excitation of the resonant frequencies in the considered domain while not being mixed with them, especially in the coalescence regime.

Parametric amplification and frequency mixing in coupled circuits have been reported in very early works [56,57], where the spatiotemporal modulation of two coupled transmission lines can convert energy between waves of different frequencies. A similar amplification effect can be realized here in the mechanical system via the time modulation process acting as gain or loss. In Figs. 2(b)–2(f), we illustrate the system's vibration response when we fix $\alpha = 0.2$ and select five values of ω_m, marked as circles in Fig. 2(a). At the frequencies of $\omega_m/\omega_0 = 1.7$ and 2.3, in the white area of Fig. 2(a), the response amplitudes are within a bounded range that proves the stability of the system. In contrast, at $\omega_m/\omega_0 = 2$
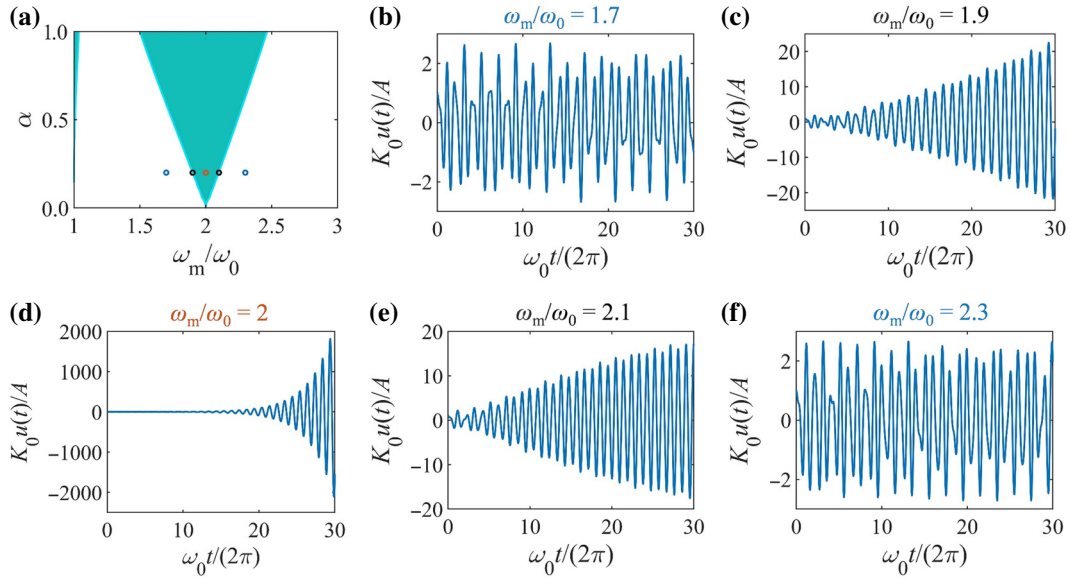
FIG. 2. (a) Transition curves obtained by Mathieu equation, the unstable regions ($g > 2$) are color-filled, while the other white regions represent the stability of the system. The blue, black, and orange circles mark different ω_m with $\alpha = 0.2$, as illustrated in (b)–(f). The forced response over time with $\alpha = 0.2$ at (b) $\omega_m/\omega_0 = 1.7$, (c) $\omega_m/\omega_0 = 1.9$, (d) $\omega_m/\omega_0 = 2$, (e) $\omega_m/\omega_0 = 2.1$, (f) $\omega_m/\omega_0 = 2.3$.

and its vicinity, where the eigenfrequencies of the system coalesce, the response function exhibits an increasing exponential behavior over time, which confirms the instability of the system. Finally, at the two EPs [$\omega_m/\omega_0 = 1.9$ in Figs. 2(c) and 2.1 in 2(e)] that fall on the transition curves of Fig. 2(a), the vibration amplitudes show intermediate states between oscillations with a bounded range and exponential growth. Similar features at EPs that can be explained with nonreciprocal coupling are demonstrated in acoustic and circuit systems with time modulation [47,58]. In Fig. 9 of Appendix B, we show the results of solving the Mathieu equation in a wider range of ω_m/ω_0 from 0 to 3.

It should be mentioned that when the eigenvalues are real, the total energy and displacement amplitude of the system are constant (such as in a simple harmonic or a periodic motion). In contrast, complex eigenvalues imply gain and loss, which are reflected in the variation of the energy and the increase in the amplitude of some solutions over time. In fact, this is consistent with the results given by the Mathieu equation in Fig. 2; that is, the system is stable in the region of real eigenvalues [Figs. 2(b) and 2(f)], and becomes unstable in the region of complex eigenvalues [Fig. 2(d)]. The EPs are on the transition curves between the stability and instability areas and the vibration responses increase slightly over time [Figs. 2(c) and 2(e)]. Thus, these two methods provide similar physical conclusions.

IV. THEORETICAL AND SIMULATION RESULTS OF RESPONSE SPECTRA

Under the external excitation force applied on the mass, we calculate the theoretical time responses in the normalized time domain of $\omega_0 t/(2\pi) = 500$, with ω_m/ω_0 ranging from 1.7 to 2.3 and $\alpha = 0.2$, then do the Fourier transform to get the results in the frequency domain. The parameters of the excitation force $F(t) = A \sin(\omega_c t)$ are the same as in Sec. III. Figure 3(b) shows that the response peaks from bifurcation to coalescence and then to rebifurcation are consistent with the evolution of the eigenfrequencies in Fig. 1(d); the positions of the resonant peaks are represented by red dots. The magnitudes of the responses along the z axis of the diagram have been normalized with respect to their own peak for each modulation parameter of ω_m/ω_0. The peaks around the frequency of $1.5\omega_0$ that are indicated by the red arrow are aroused by the applied excitation force, and the peaks of the fundamental modes at ω_0 are generally higher than those of first-order harmonic modes. At the two EPs of $\omega_m/\omega_0 = 1.9$ and 2.1, the two peaks of fundamental and first-order harmonic modes coalesce at the eigenfrequency of $\omega_m/2$. In the coalescing phase, the response peaks become smoother because of the attenuation effect caused by the imaginary parts of the eigenfrequencies. The vibration amplitude that increases exponentially over time would be more dominant than the excitation amplitude if we selected a long enough time domain, so that the peaks at the excitation frequency would vanish in the coalescing phase.

We also build a three-dimensional (3D) finite-element model equivalent to the theoretical model, as shown in Fig. 3(a). The upper cylindrical block analogous to the mass is made of tungsten (Young's modulus $E_1 = 360$ GPa, density $\rho = 17\,800$ kg/m^3, Poisson's ratio $v = 0.28$), the lower cylindrical patch analogous to the spring is made of magnesium (Young's modulus $E_2 = 45$ GPa, density $\rho = 1770$ kg/m^3, Poisson's ratio $v = 0.35$), their radii are
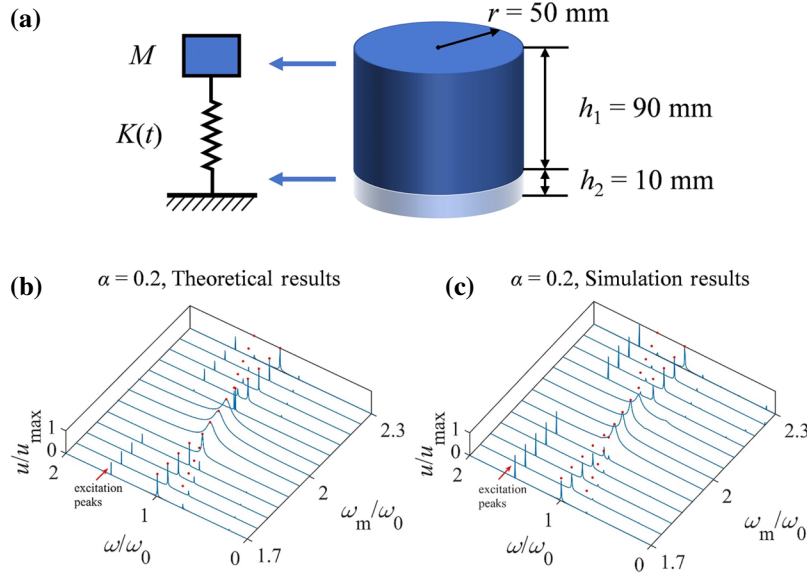
FIG. 3. (a) Schematic of the mass-spring oscillator (theoretical model) on the left. The three-dimensional finite-element model shown on the right is analogous to the theoretical model; it consists of the upper tungsten mass (blue cylinder) and the lower magnesium spring (white cylinder). (b) Theoretical normalized response spectrum with ω_m/ω_0 from 1.7 to 2.3 when $\alpha = 0.2$. (c) Simulated normalized response spectrum with ω_m/ω_0 from 1.7 to 2.3 when $\alpha = 0.2$. The red dots mark the positions of the resonant peaks.

both 50 mm, and their heights are 90 and 10 mm, respectively. We introduce time variation into the Young's modulus of the magnesium patch as $E(t) = E_2[1 + \alpha \cos(\omega_m t)]$ to realize time-varying stiffness, where $\alpha = 0.2$. The excitation force is applied on the tungsten cylinder's top surface, and the responses are detected at the same position. In Fig. 3(c), the simulated response spectrum agrees well with the theoretical result. It should be noted that in the theoretical model, the excitation force is vertically applied and only the vertical motion is considered. Therefore, in the simulation, we select the first-occurring vertically vibrated mode of the tungsten cylinder as the fundamental mode with eigenfrequency $\omega_0 = 2\pi \times 8012$ Hz $= 50\,341$ rad/s. The two EPs are at $\omega_m/\omega_0 = 1.92$ and 2.1, and the small deviations from the theoretical results could come from the errors generated by the simulation process and the equivalent 3D modeling of the mass-spring oscillator.

V. EP INDUCED BY AN OSCILLATOR WITH TIME-VARYING STIFFNESS AND CONSTANT DAMPING

Next, we consider a mass-spring system with damping c as shown in Fig. 4(a) and described by the following equation of motion:

$$M\frac{d^2u(t)}{dt^2} + c\frac{du(t)}{dt} + K(t)u(t) = 0. \quad (13)$$

We define a dimensionless damping ratio $\zeta = c/(2\sqrt{K_0 M})$. We again set the state vector as $\mathbf{s} = [du/dt, u]^T$, and the

Hamiltonian $\mathbf{H}(t)$ of Eq. (2) becomes

$$\mathbf{H}(t) = \begin{bmatrix} -\dfrac{c}{M} & -\dfrac{1}{M}K(t) \\ 1 & 0 \end{bmatrix}. \quad (14)$$

The subsequent procedures to solve the eigenvalue problem are the same as in the undamped case in Sec. II. We first study the case of constant stiffness ($\alpha = 0$) with a damping ratio $\zeta = 0.2$. As shown in Fig. 4(b), the two evolution curves intersect at a smaller modulation frequency of $\omega_m/\omega_0 = 1.96$ compared with the undamped case. Meanwhile, the intersection is at $\omega/\omega_0 = 0.98$ and can be explained by the expression of the damped fundamental frequency, which is given by $\omega = \omega_0\sqrt{1 - \zeta^2}$. Then we introduce the time-varying stiffness with $\alpha = 0.2$ and $\zeta = 0.2$, as shown in Fig. 4(c). The calculated complex eigenfrequency spectrum is shown in Figs. 4(d) and 4(e), and $|\det(\mathbf{W})|$ [$\mathbf{W}$ is the associated eigenvector matrix as defined after Eq. (10)] is shown in Fig. 4(f). The coalescing phase, with imaginary parts in the eigenfrequencies, symmetrically expands to both sides of $\omega_m/\omega_0 = 1.96$, and the two EPs occur at $\omega_m/\omega_0 = 1.83$ and 2.09. Compared with the undamped case, the damping of the system leads to a wider coalescent frequency range and lower center frequency of the coalescing phase. Outside the coalescent phase, the imaginary parts of the eigenfrequency are at $\text{Im}(\omega/\omega_0) = 0.2$. The periodic solutions with a wider sweeping range of ω_m/ω_0 from 0 to 3 are presented in Appendix C.
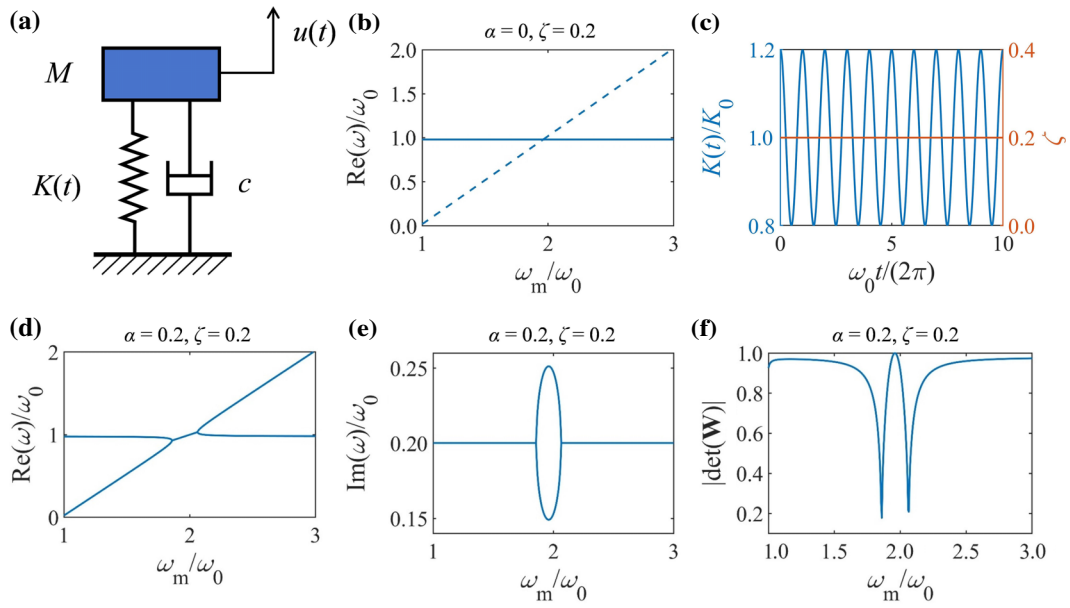
FIG. 4.   (a) Schematic of the mass-spring model with constant mass M, time-varying stiffness $K(t)$, and constant damping c. (b) The variation of the real parts of the eigenfrequencies as a function of $\omega_{\mathrm{m}}/\omega_0$ when $\alpha = 0$, damping ratio $\zeta = 0.2$. (c) Schematic of the time-varying stiffness with $\alpha = 0.2$, $\zeta = 0.2$ ($c = 0.4$ N s/m). The variation of the (d) real and (e) imaginary parts of the eigenfrequencies and (f) |det($\mathbf{W}$)| ($\mathbf{W}$ is the associated eigenvector matrix) as a function of $\omega_{\mathrm{m}}/\omega_0$ when $\alpha = 0.2$, $\zeta = 0.2$.

We explore the response spectra under the excitation force $F(t) = A \sin(\omega_{\mathrm{c}}t)$ with different damping ratios ζ when $\alpha = 0.2$ and $\omega_{\mathrm{c}} = 1.5\omega_0$. As shown in Figs. 5(a)–5(c), the results are selected at three values of $\omega_{\mathrm{m}}/\omega_0 = 1.7$, 2, 2.3 rad/s, including before, within, and after the coalescing phase. When $\omega_{\mathrm{m}}/\omega_0 = 1.7$ and 2.3, the resonant peaks become broader and the peaks at the excitation frequency vanish as the damping ratio increases. In the coalescing phase with $\omega_{\mathrm{m}}/\omega_0 = 2$, the response peak gets broader as the damping ratio increases. The theoretical response
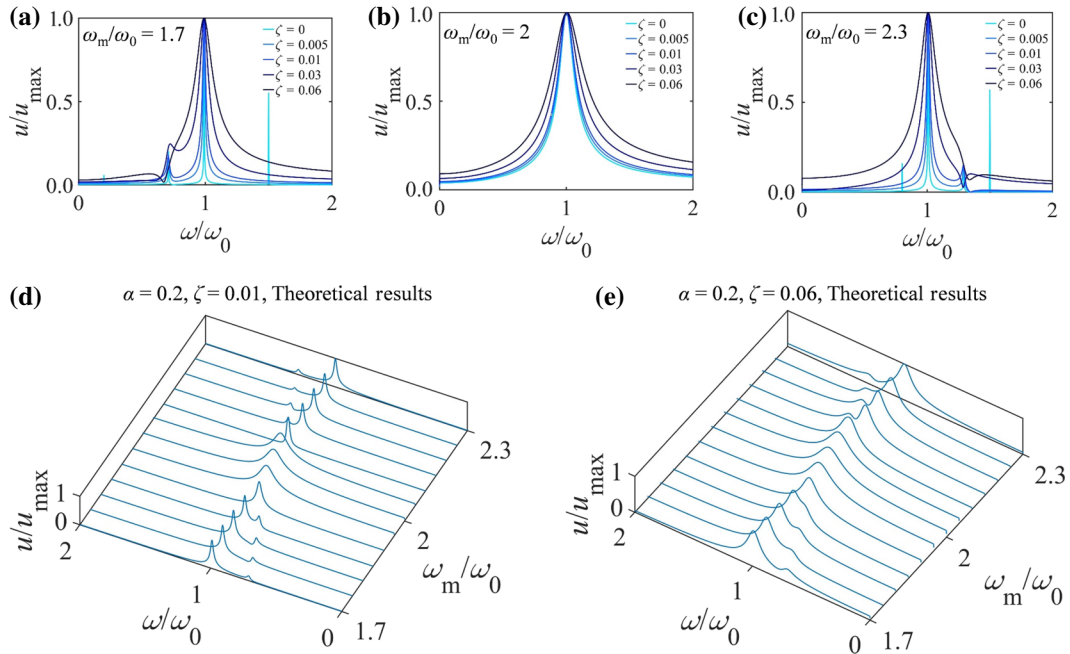

FIG. 5.   Response curves with different damping ratios ζ and $\alpha = 0.2$ when (a) $\omega_{\mathrm{m}}/\omega_0 = 1.7$, (b) $\omega_{\mathrm{m}}/\omega_0 = 2$, (c) $\omega_{\mathrm{m}}/\omega_0 = 2.3$. Theoretical normalized response spectra when $\alpha = 0.2$ and (d) $\zeta = 0.01$, (e) $\zeta = 0.06$ with $\omega_{\mathrm{m}}/\omega_0$ from 1.7 to 2.3.

spectra at $\zeta = 0.01$ and 0.06 with ω_m/ω_0 from 1.5 to 2.5 are shown in Figs. 5(d) and 5(e), respectively. Owing to the damping, response peaks at the excitation frequency between the two eigenfrequencies do not appear, as explained above, and the harmonic resonant peaks can hardly be seen when $\zeta = 0.06$.

VI. DETECTION OF PERTURBATION MASS AT THE EP

One of the significant properties of the EP is the enhanced sensitivity for the detection of small perturbations. When a perturbation is introduced into the system with an EP, the degeneracy will be lifted with a bifurcation of the coalesced eigenfrequencies and a frequency splitting. The splitting has a square-root relationship with the perturbation, which exhibits an enhanced sensitivity compared with the linear responses in conventional resonant structures [9,25]. We introduce the perturbation in the mass term of the equation of motion [Eq. (1)] as $M(1+\eta)$, where η is the perturbation, and select the EP at $\omega_m/\omega_0 = 2.1$ to explore its detection. In Figs. 6(a) and 6(b), we show the splitting of the eigenfrequencies under increasing perturbation theoretically at two values of the damping, $\zeta = 0$ and 0.01. The insets of the figures represent the splitting in a logarithmic scale in order to extract the slope at the origin. The slopes are close to 0.5 and demonstrate the square-root behavior of the splitting.

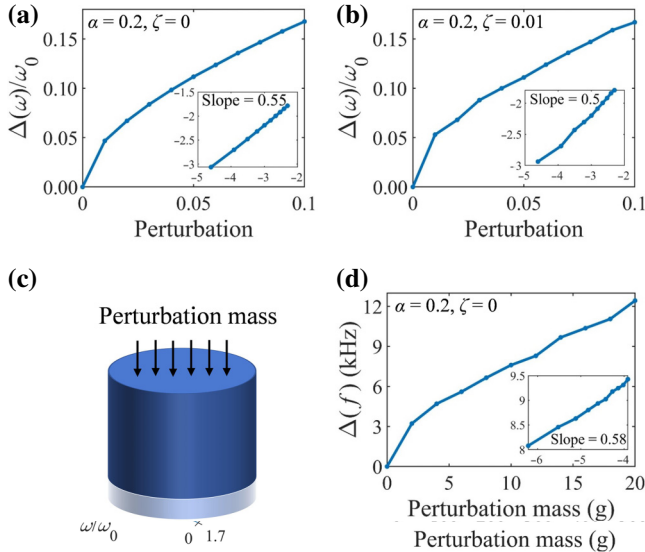Then a 3D finite-element simulation is conducted with the same model as in Sec. IV. The EP at $\omega_m/\omega_0 = 2.1$ is selected to study the frequency splitting under perturbation in the form of added mass applied on the tungsten cylinder's top surface, as shown in Fig. 6(c). The frequency splitting and logarithmic results are shown in Fig. 6(d): the slope has a larger deviation from 0.5 than the theoretical result because of the model calculation error but still illustrates the enhanced sensitivity.

VII. EP CONSTRUCTION AND PERTURBATION DETECTION BY PIEZOELECTRIC SCHEME

In this section, we propose a practical and feasible solution method to realize an EP in a time-varying system. The design is based on shunted piezoelectric patches to produce the analogue of a spring with time-varying stiffness. As shown in Fig. 7(a), the upper cylinder refers to the tungsten mass, while the lower cylinder refers to the piezoelectric patch. The piezoelectric patch is made of PZT-4 (Lead zirconate titanate), and the external circuit consists of a switch and a negative capacitance subcircuit, which can lead to the variation of the equivalent modulus [53]. The parameters of the PZT-4 patch and the circuit are shown in Table I. The piezoelectric coupling coefficient of the PZT-4 patch with strain and polarization both along the thickness direction is $k_{33} = 0.7$, C_p^T is the stress-free capacitance under constant force, which equals 0, and $C_p^S = C_p^T(1 - k_{33}{}^2)$ is the strain-free capacitance under constant extension, which equals 0 [59].

FIG. 6. Theoretical results of the frequency splitting versus perturbation when $\alpha = 0.2$ with (a) $\zeta = 0$ and (b) $\zeta = 0.01$. (c) Schematic of three-dimensional finite-element model with added mass as perturbation applied on the top surface of tungsten cylinder. (d) Simulation results of the frequency splitting versus perturbation mass with $\alpha = 0.2$ and $\zeta = 0$.
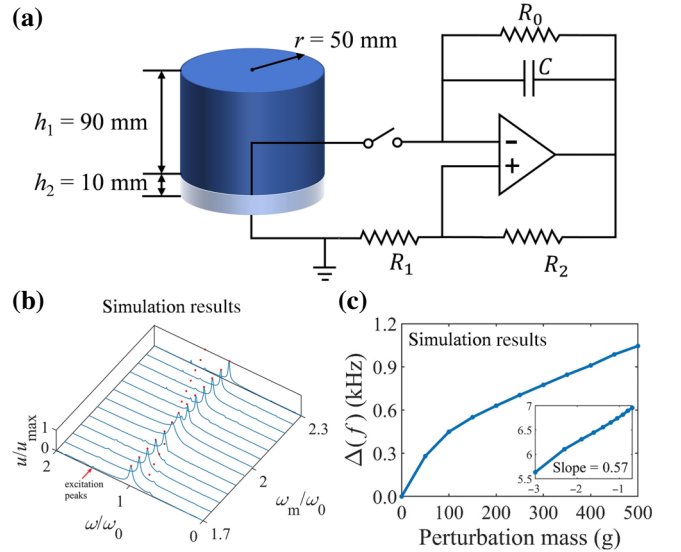

FIG. 7. (a) Schematic of the mass-spring oscillator realized by a piezoelectric mechanism, which consists of the upper tungsten mass (blue cylinder) and the lower PZT (Lead zirconate titanate) spring (white cylinder). (b) Response-normalized spectrum with ω_m/ω_0 from 1.7 to 2.3. The red dots mark the positions of the resonant peaks. (c) Simulation results of the frequency splitting versus perturbation mass.

TABLE I.   Parameters of PZT-4 patch and the shunted circuit.

Property	Value
Capacitance C	2 nF
Resistance R_0	1 MΩ
Resistance R_1	10 kΩ
Resistance R_2	15 kΩ
Piezoelectric strain constants d_{31}	-1.23×10^{-10} C/N
Piezoelectric strain constants d_{32}	2.89×10^{-10} C/N
Piezoelectric strain constants d_{33}	4.96×10^{-10} C/N
Density ρ	7500 kg/m^3
Young's modulus E_p	76.5 GPa
Strain-free capacitance C_p^S	0.92 nF
Stress-free capacitance C_p^T	1.8 nF

The obtained negative capacitance is $-C_n = -(R_2/R_1)$ $C = -3$ nF [60]. When the switch is on, the equivalent elastic modulus of the piezoelectric patch is given as follows [61]:

$$E_p^e = E_p \frac{C_n - C_p^T}{C_n - C_p^S} = E_p(1 - \alpha). \quad (15)$$

Substituting the corresponding parameters, we obtain a modulation amplitude $\alpha = 0.42$. Note that the practical scheme with a switch-controlled circuit can only realize the square-wave modulation of the modulus (the stiffness) as follows:

$$E_p^e(t) = E_p + \frac{\alpha E_p}{2}\{\text{sgn}[\cos(\omega_m t)] - 1\}. \quad (16)$$

The modulation law performs as follows: in the switch-off period, the piezoelectric patch's modulus corresponds to E_p, while in the switch-on period, it becomes E_p^e. Such square-wave modulation is different from the cosine form in the former sections, but it can still exhibit the EP phenomenon with the similar modulation frequency. The eigenfrequency with vertical displacement mode is $\omega_0 = 2\pi \times 10\,536$ Hz $= 66\,200$ rad/s. In the range of modulation frequency from $1.7\omega_0$ to $2.3\omega_0$, we get the simulated response spectrum shown in Fig. 7(b). One can note that the center frequency of the coalescing phase is lower than $\omega_m/\omega_0 = 2$ with the two EPs at $\omega_m/\omega_0 = 1.914$ and 2.006, and the peaks are attenuated compared with the simulated results in Fig. 3(c). The lowering and attenuation result from the damping effect induced by the oscillation circuit. We choose the EP at $\omega_m/\omega_0 = 2.006$ to explore the capability of detecting the perturbation. Figure 7(c) shows the splitting frequency as a function of a mass added on the top surface of the tungsten cylinder. The logarithmic presentation in the inset confirms the close to square-root behavior in the range of a small perturbation.

VIII. CONCLUSION

In summary, we have investigated the EP phenomenon in a mass-spring oscillator with the time-varying stiffness. By using the space-state method to solve the eigenfrequency problem, we found that the second-order EP results from the coupling of the fundamental and harmonic modes. The solutions of the Mathieu equation indicate the connection between the EP and the stability threshold of the system. Then a constant damping was introduced, which can lead to a wider range and lower center frequency of the coalescing phase. The theoretical results of the response spectra illustrate the damping's attenuation effect on the
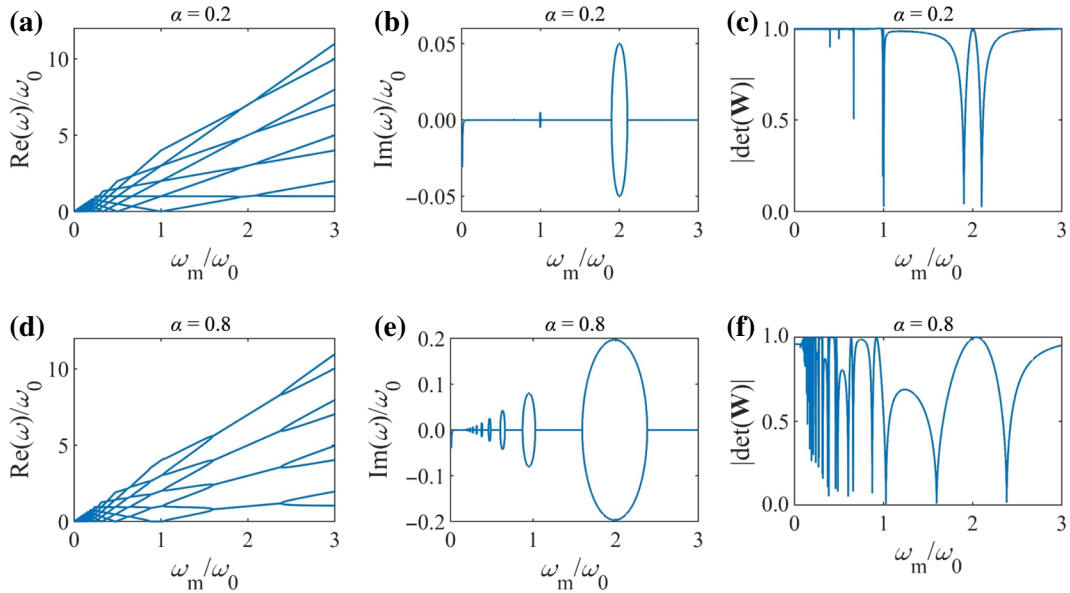

FIG. 8.   The periodic solutions of (a) real and (b) imaginary parts of the eigenfrequencies and (c) $|\det(\mathbf{W})|$ ($\mathbf{W}$ is the associated eigenvector matrix) versus ω_m/ω_0 from 0 to 3 when $\alpha = 0.2$. Panels (d)–(f) present results similar to those in (a)–(c) when $\alpha = 0.8$.

resonance and excitation peaks. In addition, the 3D finite-element model of the undamped case with time-varying modulus was conducted to obtain the response spectrum and found to agree well with the theoretical results. A mass added as a perturbation was introduced to study the detection capability of the EP and the enhanced sensitivity. Theoretical and simulated results demonstrate the square-root behavior of the frequency splitting versus the perturbation. We also proposed a practical scheme to realize equivalent periodically time-varying stiffness in the square-wave form, realized via piezoelectric patch shunts with a switchable negative capacitance circuit. The response spectrum shows the EP phenomenon, proving the feasibility and showing that the frequency splitting under added mass also exhibits enhanced sensitivity. Our work may inspire studies and applications in the elastic wave field, for instance, in wave control by artificial structures [62,63], space-time modulated metamaterials [46,50], high-sensitivity sensing [22,23], and so on. Several interesting opportunities are identified for future studies, such as novel schemes to construct time-varying mechanical systems, other modulation functions, higher-order EPs, and a method for detecting tiny cracks.

ACKNOWLEDGMENTS
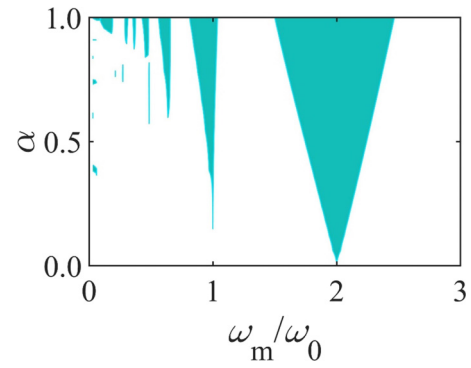
FIG. 9. Transition curves obtained by the Mathieu equation in the range of ω_m/ω_0 from 0 to 3.

APPENDIX A: PERIODIC SOLUTIONS OF THE UNDAMPED CASE IN THE RANGE OF ω_m/ω_0 FROM 0 TO 3

We obtain the periodic solutions of the eigenfrequency spectra as shown in Fig. 8. The complex eigenfrequencies have a period of ω_m and share the same imaginary parts. In the range of ω_m/ω_0 from 0 to 1, infinite EPs can be found and the frequency ranges of the coalescing phases get
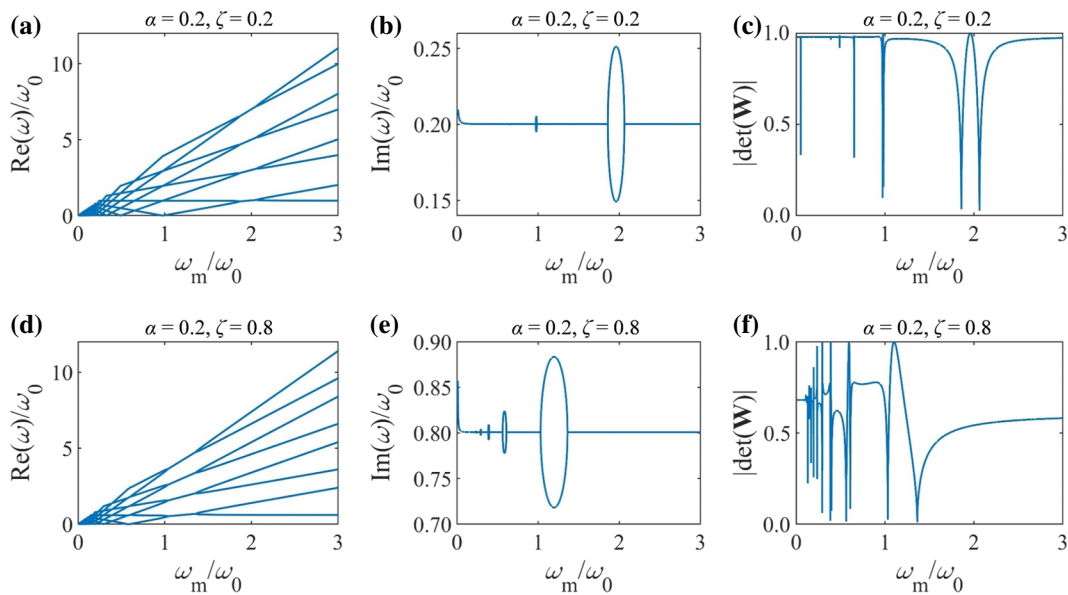
FIG. 10. The periodic solutions of (a) real and (b) imaginary parts of the eigenfrequencies and (c) |det(**W**)| (**W** is the associated eigenvector matrix) versus ω_m/ω_0 from 0 to 3 when $\alpha = 0.2$, $\zeta = 0.2$. Panels (d)–(f) present results similar to those in (a)–(c) when $\alpha = 0.8$, $\zeta = 0.2$.

smaller as ω_m/ω_0 decreases. When the modulation amplitude α increases, the imaginary parts of the eigenfrequencies in the coalescing phases enlarge and the corresponding maximum values increase.

APPENDIX B: TRANSITION CURVES IN THE RANGE OF ω_m/ω_0 FROM 0 TO 3

As shown in Fig. 9, infinite unstable regions emerge when ω_m/ω_0 is smaller than 1. This is consistent with the infinite coalescing phases depicted in Appendix A. As α increases, the ranges of the unstable regions become wider, which is also consistent with the conclusion in Appendix A.

APPENDIX C: PERIODIC SOLUTIONS OF THE DAMPED CASE IN THE RANGE OF ω_m/ω_0 FROM 0 TO 3

We present the periodic complex eigenfrequency spectra of the damped case in Fig. 10. In the range of ω_m/ω_0 from 0 to 1, infinite EPs can be found and the frequency ranges of the coalescing phases get smaller as ω_m/ω_0 decreases. When the damping ratio ζ increases, the coalescing phases of spectra enlarge, the corresponding maximum values of the imaginary parts increase, and the center frequencies of the coalescing phases decrease.

---

[1] C. Scheibner, W. T. M. Irvine, and V. Vitelli, Non-Hermitian band topology and skin modes in active elastic media, Phys. Rev. Lett. **125**, 118001 (2020).

[2] H. Xue, Q. Wang, B. Zhang, and Y. D. Chong, Non-Hermitian Dirac cones, Phys. Rev. Lett. **124**, 236403 (2020).

[3] R. El-Ganainy, K. G. Makris, M. Khajavikhan, Z. H. Musslimani, S. Rotter, and D. N. Christodoulides, Non-Hermitian physics and PT symmetry, Nat. Phys. **14**, 11 (2018).

[4] E. J. Bergholtz, J. C. Budich, and F. K. Kunst, Exceptional topology of non-Hermitian systems, Rev. Mod. Phys. **93**, 015005 (2021).

[5] Z. Zhang, M. Rosendo Lopez, Y. Cheng, X. Liu, and J. Christensen, Non-Hermitian sonic second-order topological insulator, Phys. Rev. Lett. **122**, 195501 (2019).

[6] L. Cao, Y. Zhu, S. Wan, Y. Zeng, and B. Assouar, On the design of non-Hermitian elastic metamaterial for broadband perfect absorbers, Int. J. Eng. Sci. **181**, 103768 (2022).

[7] L. He, Y. Li, B. Djafari-Rouhani, and Y. Jin, Hermitian and non-Hermitian Weyl physics in synthetic three-dimensional piezoelectric phononic beams, Phys. Rev. Res. **5**, 023020 (2023).

[8] K. Ding, G. Ma, M. Xiao, Z. Q. Zhang, and C. T. Chan, Emergence, coalescence, and topological properties of multiple exceptional points and their experimental realization, Phys. Rev. X **6**, 021007 (2016).

[9] R. Cai, Y. Jin, Y. Li, T. Rabczuk, Y. Pennec, B. Djafari-Rouhani, and X. Zhuang, Exceptional points and skin modes in non-Hermitian metabeams, Phys. Rev. Appl. **18**, 014067 (2022).

[10] Y. Sun, W. Tan, H. Q. Li, J. Li, and H. Chen, Experimental demonstration of a coherent perfect absorber with PT phase transition, Phys. Rev. Lett. **112**, 143903 (2014).

[11] X. Li, Z. Yu, H. Iizuka, and T. Lee, Experimental demonstration of extremely asymmetric flexural wave absorption at the exceptional point, Extreme Mech. Lett. **52**, 101649 (2022).

[12] L. Feng, Y. L. Xu, W. S. Fegadolli, M. H. Lu, J. E. Oliveira, V. R. Almeida, Y. F. Chen, and A. Scherer, Experimental demonstration of a unidirectional reflectionless parity-time metamaterial at optical frequencies, Nat. Mater. **12**, 108 (2013).

[13] Q. Wu, Y. Chen, and G. Huang, Asymmetric scattering of flexural waves in a parity-time symmetric metamaterial beam, J. Acoust. Soc. Am. **146**, 850 (2019).

[14] K. Ding, Z. Q. Zhang, and C. T. Chan, Coalescence of exceptional points and phase diagrams for one-dimensional PT-symmetric photonic crystals, Phys. Rev. B **92**, 235310 (2015).

[15] Z. Gu, H. Gao, P.-C. Cao, T. Liu, X.-F. Zhu, and J. Zhu, Controlling sound in non-Hermitian acoustic systems, Phys. Rev. Appl. **16**, 057001 (2021).

[16] R. Fleury, D. Sounas, and A. Alu, An invisible acoustic sensor based on parity-time symmetry, Nat. Commun. **6**, 6905 (2015).

[17] Z. Lin, H. Ramezani, T. Eichelkraut, T. Kottos, H. Cao, and D. N. Christodoulides, Unidirectional invisibility induced by PT-symmetric periodic structures, Phys. Rev. Lett. **106**, 213901 (2011).

[18] L. Feng, Z. J. Wong, R.-M. Ma, Y. Wang, and X. Zhang, Single-mode laser by parity-time symmetry breaking, Science **346**, 972 (2014).

[19] J. Doppler, A. A. Mailybaev, J. Bohm, U. Kuhl, A. Girschik, F. Libisch, T. J. Milburn, P. Rabl, N. Moiseyev, and S. Rotter, Dynamically encircling an exceptional point for asymmetric mode switching, Nature **537**, 76 (2016).

[20] H. Hodaei, A. U. Hassan, S. Wittek, H. Garcia-Gracia, R. El-Ganainy, D. N. Christodoulides, and M. Khajavikhan, Enhanced sensitivity at higher-order exceptional points, Nature **548**, 187 (2017).

[21] J. Wiersig, Enhancing the sensitivity of frequency and energy splitting detection by using exceptional points: Application to microcavity sensors for single-particle detection, Phys. Rev. Lett. **112**, 203901 (2014).

[22] P. Djorwe, Y. Pennec, and B. Djafari-Rouhani, Exceptional point enhances sensitivity of optomechanical mass sensors, Phys. Rev. Appl. **12**, 024002 (2019).

[23] M. De Carlo, F. De Leonardis, R. A. Soref, L. Colatorti, and V. M. N. Passaro, Non-Hermitian sensing in photonics and electronics: A review, Sensors (Basel) **22**, 3977 (2022).

[24] H. Zhao, Z. Chen, R. Zhao, and L. Feng, Exceptional point engineered glass slide for microscopic thermal mapping, Nat. Commun. **9**, 1764 (2018).

[25] M. I. N. Rosa, M. Mazzotti, and M. Ruzzene, Exceptional points and enhanced sensitivity in PT-symmetric continuous elastic media, J. Mech. Phys. Solids **149**, 104325 (2021).

[26] R. Cai, Y. Jin, Y. Li, J. Zhu, H. Zhu, T. Rabczuk, and X. Zhuang, Absorption-lasing effects and exceptional points in parity-time symmetric non-Hermitian metaplates, J. Sound Vib. **555,** 117710 (2023).

[27] J. Wiersig, Structure of whispering-gallery modes in optical microdisks perturbed by nanoparticles, Phys. Rev. A **84,** 063828 (2011).

[28] J. Wiersig, Sensors operating at exceptional points: General theory, Phys. Rev. A **93,** 033809 (2016).

[29] W. Chen, S. Kaya Ozdemir, G. Zhao, J. Wiersig, and L. Yang, Exceptional points enhance sensing in an optical microcavity, Nature **548,** 192 (2017).

[30] Y. Jin, W. Li, B. Djafari-Rouhani, Y. Li, and Y. Xiang, Exceptional points for crack detection in non-Hermitian beams, J. Sound Vib. **572,** 118162 (2024).

[31] Z. Xiao, H. Li, T. Kottos, and A. Alù, Enhanced sensing and nondegraded thermal noise performance based on PT-symmetric electronic circuits with a sixth-order exceptional point, Phys. Rev. Lett. **123,** 213901 (2019).

[32] M. Moghaddaszadeh, M. A. Attarzadeh, A. Aref, and M. Nouh, Complex spatiotemporal modulations and non-Hermitian degeneracies in PT-symmetric phononic materials, Phys. Rev. Appl. **18,** 044013 (2022).

[33] V. Pacheco-Peña and N. Engheta, Effective medium concept in temporal metamaterials, Nanophotonics **9,** 379 (2020).

[34] J. R. Zurita-Sánchez, P. Halevi, and J. C. Cervantes-González, Reflection and transmission of a wave incident on a slab with a time-periodic dielectric function $\varepsilon(t)$, Phys. Rev. A **79,** 053821 (2009).

[35] Q. Wu, H. Chen, H. Nassar, and G. Huang, Non-reciprocal Rayleigh wave propagation in space–time modulated surface, J. Mech. Phys. Solids **146,** 104196 (2021).

[36] J. Park, H. Cho, S. Lee, K. Lee, K. Lee, H. C. Park, J.-W. Ryu, N. Park, S. Jeon, and B. Min, Revealing non-Hermitian band structure of photonic Floquet media, Sci. Adv. **8,** eabo6220 (2022).

[37] L. Zhang, X. Q. Chen, S. Liu, Q. Zhang, J. Zhao, J. Y. Dai, G. D. Bai, X. Wan, Q. Cheng, G. Castaldi, V. Galdi, and T. J. Cui, Space-time-coding digital metasurfaces, Nat. Commun. **9,** 4334 (2018).

[38] Z. Chen, Y. Peng, H. Li, J. Liu, Y. Ding, B. Liang, X.-F. Zhu, Y. Lu, J. Cheng, and A. Alù, Efficient nonreciprocal mode transitions in spatiotemporally modulated acoustic metamaterials, Sci. Adv. **7,** eabj1198 (2021).

[39] J. Li, C. Shen, X. Zhu, Y. Xie, and S. A. Cummer, Nonreciprocal sound propagation in space-time modulated media, Phys. Rev. B **99,** 144311 (2019).

[40] H. Nassar, X. C. Xu, A. N. Norris, and G. L. Huang, Modulated phononic crystals: Non-reciprocal wave propagation and Willis materials, J. Mech. Phys. Solids **101,** 10 (2017).

[41] C. Shen, X. Zhu, J. Li, and S. A. Cummer, Nonreciprocal acoustic transmission in space-time modulated coupled resonators, Phys. Rev. B **100,** 054302 (2019).

[42] G. Trainiti and M. Ruzzene, Non-reciprocal elastic wave propagation in spatiotemporal periodic structures, New J. Phys. **18,** 083047 (2016).

[43] M. A. Attarzadeh, J. Callanan, and M. Nouh, Experimental observation of nonreciprocal waves in a resonant metamaterial beam, Phys. Rev. Appl. **13,** 021001 (2020).

[44] J. Huang and X. Zhou, Non-reciprocal metamaterials with simultaneously time-varying stiffness and mass, J. Appl. Mech. **87,** 071003 (2020).

[45] T. T. Koutserimpas, A. Alù, and R. Fleury, Parametric amplification and bidirectional invisibility in PT-symmetric time-Floquet systems, Phys. Rev. A **97,** 013839 (2018).

[46] X. Wen, X. Zhu, A. Fan, W. Y. Tam, J. Zhu, H. W. Wu, F. Lemoult, M. Fink, and J. Li, Unidirectional amplification with acoustic non-Hermitian space−time varying metamaterial, Commun. Phys. **5,** 18 (2022).

[47] H. Kazemi, M. Y. Nada, T. Mealy, A. F. Abdelshafy, and F. Capolino, Exceptional points of degeneracy induced by linear time-periodic variation, Phys. Rev. Appl. **11,** 014007 (2019).

[48] J. Yuan, L. Geng, J. Huang, Q. Guo, J. Yang, G. Hu, and X. Zhou, Exceptional points induced by time-varying mass to enhance the sensitivity of defect detection, Phys. Rev. Appl. **18,** 064055 (2022).

[49] T. T. Koutserimpas and R. Fleury, Electromagnetic fields in a time-varying medium: Exceptional points and operator symmetries, IEEE Trans. Antennas Propag. **68,** 6717 (2020).

[50] Q. Wu, H. Qian, Y. Chen, and G. Huang, Dynamic phononic crystals with spatially and temporally modulated circuit networks, Acta Mech. Sin. **39,** 723007 (2023).

[51] J. Marconi, E. Riva, G. Di Ronco, G. Cazzulani, F. Braghin, and M. Ruzzene, Experimental observation of nonreciprocal band gaps in a space-time-modulated beam using a shunted piezoelectric array, Phys. Rev. Appl. **13,** 031001 (2020).

[52] Y. Chen, X. Li, H. Nassar, A. N. Norris, C. Daraio, and G. Huang, Nonreciprocal wave propagation in a continuum-based metamaterial with space-time modulated resonators, Phys. Rev. Appl. **11,** 064052 (2019).

[53] G. Trainiti, Y. Xia, J. Marconi, G. Cazzulani, A. Erturk, and M. Ruzzene, Time-periodic stiffness modulation in elastic metamaterials for selective wave filtering: Theory and experiment, Phys. Rev. Lett. **122,** 124301 (2019).

[54] A. Palermo, P. Celli, B. Yousefzadeh, C. Daraio, and A. Marzani, Surface wave non-reciprocity via time-modulated metamaterials, J. Mech. Phys. Solids **145,** 104181 (2020).

[55] I. Kovacic, R. Rand, and S. Mohamed Sah, Mathieu's equation and its generalizations: Overview of stability charts and their features, Appl. Mech. Rev. **70,** 020802 (2018).

[56] P. K. Tien, Parametric amplification and frequency mixing in propagating circuits, J. Appl. Phys. **29,** 1347 (1958).

[57] P. K. Tien and H. Suhl, A traveling-wave ferromagnetic amplifier, Proc. IRE **46,** 700 (1958).

[58] J. Li, Y. Jing, and S. A. Cummer, Nonreciprocal coupling in space-time modulated systems at exceptional points, Phys. Rev. B **105,** L100304 (2022).

[59] B. de Marneffe and A. Preumont, Vibration damping with negative capacitance shunts: Theory and experiment, Smart Mater. Struct. **17,** 035015 (2008).

[60] B. S. Beck, K. A. Cunefare, and M. Collet, The power output and efficiency of a negative capacitance shunt for

vibration control of a flexural system, Smart Mater. Struct. **22**, 065009 (2013).

[61] S. Behrens, A. J. Fleming, and S. O. R. Moheimani, A broadband controller for shunt piezoelectric damping of structural vibration, Smart Mater. Struct. **12**, 18 (2003).

[62] Y. Jin, L. He, Z. Wen, B. Mortazavi, H. Guo, D. Torrent, B. Djafari-Rouhani, T. Rabczuk, X. Zhuang, and Y. Li,

Intelligent on-demand design of phononic metamaterials, Nanophotonics. **11**, 439 (2022).

[63] Y. Jin, Y. Pennec, B. Bonello, H. Honarvar, L. Dobrzynski, B. Djafari-Rouhani, and M. I. Hussein, Physics of surface vibrational resonances: Pillared phononic crystals, metamaterials, and metasurfaces, Rep. Prog. Phys. **84**, 086502 (2021).